Queries

1. AU: If figures need to be replaced because of accuracy or clarity concerns, please upload each revised figure as an individual PDF at the desired final size. Figures with multiple parts should be combined in one file.

2. AU: A mismatch has been discovered between the e-mail address in the manuscript and the e-mail address in Prism. Please let us know if the e-mail address in the manuscript should be changed.

3. AU: Please expand the acronyms "TV," "PSNR," and "SSIM" on first occurrences.

4. AU: Please provide the model in "(Thorlabs; model:)."

5. AU: You did not provide funding information at the time of article submission. If this article was funded by one or more organization(s)/institutions(s), please provide the full name of that entity as provided in the Open Funder Registry (https://search.crossref.org/funding) and all pertinent grant/contract/project/award numbers.

6. AU: The Data Availability Statement for this article has been generated automatically. Please check it carefully. If any information needs to be corrected or added, please provide us with an updated statement.

7. AU: Please confirm the issue numbers added to Refs. [15,27,28].

Research Article | Vol. 40, No. 5 / May 2023 / Journal of the Optical Society of America A | 1

Journal of the Optical Society of America A
OPTICS, IMAGE SCIENCE, AND VISION

Single-shot extended field of view imaging system by point spread function engineering

RITIKA MALIK[1] AND KEDAR KHARE[1,2,*]

[1]Department of Physics, Indian Institute of Technology Delhi, New Delhi 110016, India
[2]Optics and Photonics Centre, Indian Institute of Technology Delhi, New Delhi 110016, India
*kedark@opc.iitd.ac.in

Received 2 January 2023; revised 1 April 2023; accepted 17 April 2023; posted 18 April 2023; published 0 MONTH 0000

We present a single-shot computational imaging system employing pupil phase engineering to extend the field of view (FOV) beyond the physical sensor limit. Our approach uses a point spread function in the form of a multiple-point impulse response (MPIR). Unlike the traditional point-to-point imaging model used by most traditional optical imaging systems, the proposed MPIR model can collect information from within and outside the sensor boundary. The detected raw image despite being scrambled can be decoded via a sparse optimization algorithm to get extended FOV imaging performance. We provide a thorough analysis of MPIR design regarding the number of impulses and their spatial extent. Increasing the number of impulses in MPIR of a given spatial extent leads to better information gathering within the detector region; however, it also reduces contrast in the data. Therefore, a trade-off between increasing the information and keeping adequate contrast in the detected data is necessary to achieve high-quality reconstruction. For generalization, we first demonstrate this trade-off with a simulation study and present experimental results on a suitably designed extended FOV imaging system. We demonstrate reconstructed images with a 4× gain in pixels over the native detection area without loss of spatial resolution. The proposed system design considerations are generic and can be applied to various imaging systems for extended FOV performance.

https://doi.org/10.1364/JOSAA.484734

1. INTRODUCTION

Computational optical imaging systems combine unconventional imaging hardware and image reconstruction algorithms to achieve imaging performance beyond what is possible with traditional imaging devices [1]. This model has enabled researchers to investigate novel system concepts, where the recorded raw data on the sensor may not have any visual similarity to the object being imaged. Traditional cameras, comprising a lens and a sensor, closely resemble the human eye. As a result, there is a point-to-point mapping between the object and the recorded image. The physical sensor extent therefore limits the field of view (FOV) of such imaging systems. In practice, the design of an imaging system involves a trade-off between the resolution and FOV [2]. An imaging system with simultaneous large FOV and high resolution is, however, desirable in several practical applications, e.g., in biomedical imaging systems such as digital pathology [3] and hematology [4], as well as commercial applications such as consumer photography [5]. Large FOV is routinely obtained in commercial digital pathology systems such as whole slide scanners by scanning the object to be imaged and then stitching the individual limited FOV images [3]. The technique is also used in panorama photography mode, which is now commonly available in most smartphone cameras. The requirement of overcoming the fundamental FOV–resolution trade-off has led to the emergence of novel system concepts such as Fourier ptychography [6] and gigapixel photography [5], which provide large FOV high-resolution imaging. Fourier ptychography is a coherent imaging technique that uses low-resolution large FOV optics and allows resolution beyond the diffraction limit by employing a diversity of plane waves for illumination. The need for sequential illumination with one plane wave at a time, however, impairs the temporal resolution of the system. Gigapixel multi-scale photography [5] utilizes a large number of cameras configured so that each camera images a local part of the overall scene, thus reducing the requirement to correct system aberrations. The pictures from multiple cameras are fused to obtain an image of nearly uniform quality across a large FOV. Gigapixel cameras are bulky, and the ultimate image resolution is decided by the individual camera lenses instead of the total system aperture. Other scan-free methods for wide FOV include the use of the Mesolens [7], compounded eye lens [8], and learned thin plate imager [9]. These prior studies have provided important insights for designing large FOV imaging systems as summarized in a recent review [10] on large space–bandwidth product (SBP) imaging.

An important system configuration for large SBP imaging is structured illumination microscopy (SIM), which achieves improved spatial resolution without changing the FOV. This is

accomplished by utilizing coded illumination, which enables the access of higher spatial frequencies outside the passband of the imaging system (as determined by the Fourier plane aperture). Our initial work [11] indicates the viability of an extended FOV imaging system analogous to SIM where the roles of spatial and Fourier space are exchanged. In particular, structuring in the Fourier space can increase the effective image capture area beyond the physical sensor limit. A specific design for such a system involves a Fourier plane filter that leads to a multiple-point impulse response (MPIR) [11,12]. The MPIR component of the system point spread function (PSF) enables the collection of object data that would otherwise be outside the sensor array's active region. The recorded image appears scrambled and visually difficult to interpret; however, it has adequate information to form an extended FOV image with an appropriate reconstruction algorithm. The main aim of this paper is to build on the conceptual ideas introduced in [11]. We provide a detailed exposition of the expected extended FOV performance with a series of MPIR designs with a varying number and spatial extent of the multiple impulses. A proximal gradient based algorithm is described that uses image sparsity ideas (in the form of a total variation penalty function) for achieving extended FOV image reconstruction. Our MPIR design considerations and the reconstruction algorithm are further tested with an experimental system that employs a phase-only spatial light modulator (SLM) device for realizing the required Fourier plane phase mask. In the context of computational imaging, pupil phase engineering concepts have been previously used mainly for extending the depth of focus using cubic phase [13] and log-asphere [14] masks, extending spectral range [15], and encoding depth information with rotating PSF [16]. Here, we add to this series of important system developments with a system design that extends the FOV of the imaging system beyond the physical sensor area with a single image capture.

The paper is organized as follows. In Section 2, we describe the basic concept behind an extended FOV system. Section 3 describes an iterative image reconstruction algorithm for extended FOV image reconstruction that utilizes image sparsity ideas. The algorithm is then used for image reconstruction with various MPIR designs later in the paper. In Section 4, we highlight two important considerations that we term as information regime and contrast regime that provide generic guidelines for selecting a specific MPIR design for good image reconstruction performance. Section 5 describes experimental results with a USAF chart object to illustrate extended FOV image recoveries. In Section 6, we provide concluding remarks and future directions.

2. EXTENDING FOV IMAGING BEYOND PHYSICAL SENSOR BOUNDARIES

To encode large FOV information into a constrained detector region, we examine an imaging system with a PSF designed to have multiple spatially separated impulses. Such a PSF can be implemented for incoherent imaging systems by adding a suitable phase mask to the imaging system's Fourier plane. We can create the phase mask via iterative Fourier transform algorithms that are now readily available along with commercially available SLM devices. Alternatively, the desired phase masks may be fabricated by lithographic procedures. In line with our discussion of the extended FOV as analogous to SIM imaging in the previous section, the distribution of impulses may be made similar to the Fourier band structure in SIM configurations [17]. Horisaki and Tanida [18] used a multiplexing scheme to improve FOV detection capability. Their work, however, achieves the increased FOV in one direction. Additionally, a thorough study is needed to determine how many impulses are needed and how they should be distributed spatially to create an extended FOV system. The issue is further addressed by employing a random convolution strategy in [19]. However, unless careful thought is given to the number of impulses and their spatial extent, the scrambled image data may not lead to optimal reconstructed image quality. Recently, Yao *et al.* [20] used a lenslet array with lenses distributed spatially in a hexagonal manner to record an image with overlapping of adjacent FOVs. These scrambled data are then directly used along with machine learning to categorize different types of cells over an extended FOV. In the following sections, we report an intuitive approach with a systematic study of the number of impulses and their distribution to illustrate these points and provide design considerations to achieve good quality extended FOV image reconstruction.

A. Extending FOV Imaging with Multiple-Point PSF

For an imaging system using a spatially incoherent illumination, the forward model for the measured intensity in the image plane is given by

$$I_{\text{out}}(\mathbf{r}) = I_{\text{in}}(\mathbf{r}) * p(\mathbf{r}) + n(\mathbf{r}). \tag{1}$$

Here, I_{out}, I_{in} represent the 2D output and input, respectively. $p(\mathbf{r})$ is the incoherent PSF of the system, which is related to the coherent impulse response $h(\mathbf{r})$ of the system through the relation

$$p(\mathbf{r}) = |h(\mathbf{r})|^2, \tag{2}$$

and $n(\mathbf{r})$ is the noise in the measurement, which is assumed to be additive. Intuitively, the simplest PSF for accessing information beyond the physical sensor boundary is the MPIR [11] as shown in Fig. 1(d). This PSF consists of spatially distributed impulses to bring information that usually goes outside the physical sensor boundary within the detection region as shown in Fig. 1(e). In its idealized form, the MPIR consists of multiple delta impulses at the locations (x_j, y_j) and may be described mathematically as

$$p(\mathbf{r}) = \sum_{j=1}^{J} a_j \delta(\mathbf{r} - \mathbf{r}_j), \tag{3}$$

where a_j is the positive valued weighting factor of the jth impulse, and J is the total number of impulses, such that $\Sigma_j a_j = 1$. In a real system, each of the delta functions above will be replaced by a diffraction-limited spot. The shift and add nature of data collected using the MPIR is expected to be better at preserving the high-spatial-frequency information compared to impulse responses with continuous functional forms over the same spatial extent. For convenience, we follow

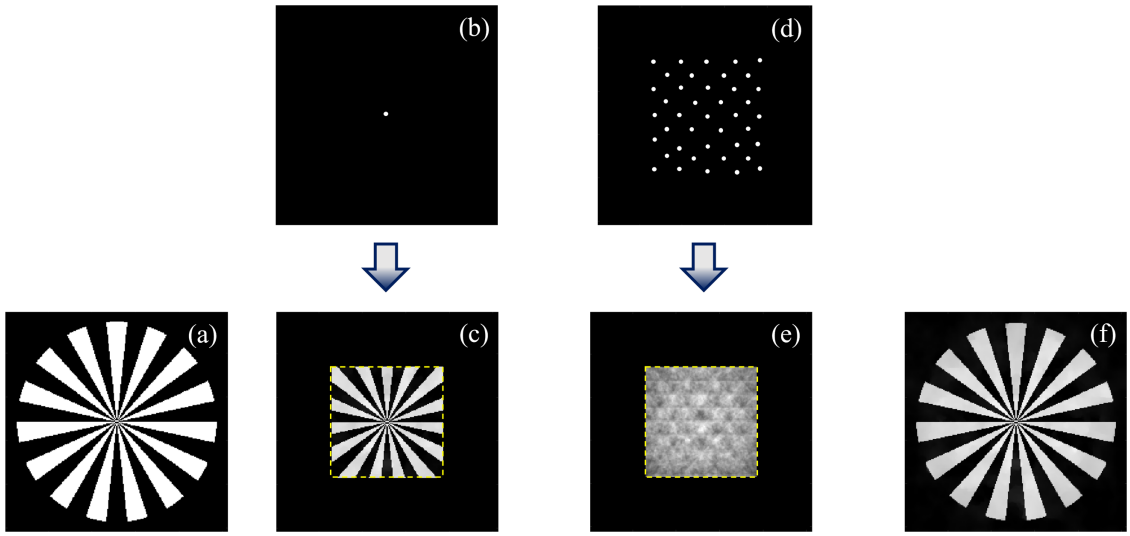

Fig. 1. Image acquisition with multiple-point impulse response (MPIR). (a) Siemens star as a target object. (b) PSF of the traditional imaging system as a single-point impulse response; (c) image captured using single-point impulse response. A yellow dotted square shows active area of the sensor, which limits the FOV of the captured image. (d) Proposed PSF configuration as multiple-point impulse response. (e) Scrambled output image recorded with MPIR on the limited size sensor shown by yellow dotted square. (f) Restored full FOV image using sparse recovery algorithm.

the lexicographic notation of linear algebra and vectorize the 2D image representation as a 1D vector. Therefore the above imaging system as described in Eq. (1) can also be written into the form of a linear system of equation as

$$y = \hat{S}\hat{A}x + \text{noise}. \tag{4}$$

As illustrated pictorially in Fig. 2, $y = I_{\text{out}} \in R^{M\times 1}$ are the measurements over a limited detector area, and $x = I_{\text{in}} \in R^{N\times 1}$ is the unknown extended FOV image. The operator $\hat{A} \in R^{N\times N}$ represents the measurement matrix that performs $2D$ convolution with MPIR in matrix form, and $\hat{S} = s_{ij} \in R^{M\times N}$ is the truncation operation over a limited detector area with entries as zero and one, applied to this system. Clearly, the number of measurements M is now less compared to the number of pixels N in the unknown extended image to be recovered. Specifically, $s_{ij} = 1$ if and only if data lie within the sensor's active area and 0 whenever outside the sensor domain.

We may note that when the imaging sensor is large enough to capture all the measurements, i.e., $M = N$, in that case, $\hat{S}$ is the identity matrix; otherwise, it has ones within the active area of the sensor and zeros elsewhere as shown in Fig. 2. The increase in the FOV of the imaging system therefore depends on the entries in the matrix $\hat{A}$. In other words, the number of impulses and their distribution control the effective FOV extension. In this work, we use an analogy from SIM systems to get insights into impulse distribution. These conditions are similar to the ones generally encountered in SIM to extend the frequency space coverage. However, we remark that the extended FOV system we describe here has certain unique aspects of its own, making it possible to get large FOV imaging performance in a single-shot operation.

3. ALGORITHM FOR EXTENDED FOV IMAGE RECOVERY

To recover the missing FOV information from the scrambled data, we formulate image reconstruction as a constrained minimization problem as follows:

$$\min \frac{1}{2}\|y - \hat{S}\hat{A}x\|_2^2 + \lambda\|x\|_{\text{TV}}. \tag{5}$$

Here, the first term represents the data fidelity (in terms of L2-norm squared error), and $\|\ \|_{\text{TV}}$ is the discrete total variation norm. We have used anisotropic total variation [21] in this work. The positive valued parameter λ is the weight between

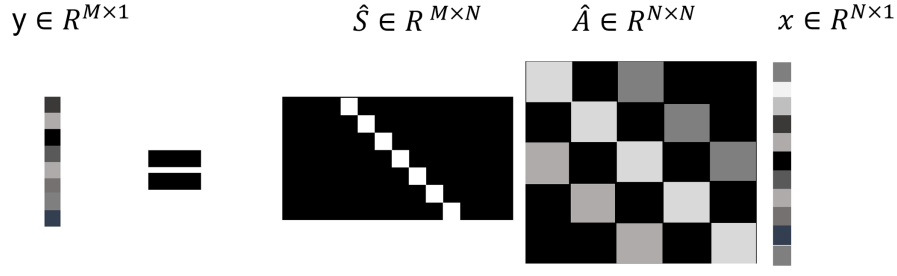

Fig. 2. Mathematical model of the proposed imaging system. A target object x gets scrambled by the measurement matrix $\hat{A}$. The scrambled measurements are then captured by the limited FOV sensor represented by truncation operator $\hat{S}$. Vector y represents the scrambled data captured with a limited FOV sensor.

the data fidelity and the constraint terms. The proximal gradient descent method is adopted to solve the above non-smooth optimization problem [22]. In this class of algorithms, the objective is split into two terms: the first is differentiable and solved by a gradient descent step, and the second is non-smooth, which is handled using the proximal operator in an alternative manner. For adaptive tuning the parameter λ during iterations, we employ a methodology inspired by the adaptive steepest descent projection onto convex sets (ASD-POCS) algorithm [23] in computed tomography and described below. This methodology has been used in an earlier work in the context of digital holography [24] as well as our earlier work on extended FOV reconstruction [11]. We initialize the iterative process with a guess solution x^0, which is the same as the measured data y and is zero-padded up to the desired extended FOV image size. In particular, if the detector size is $m \times n$ and the spatial extent of the MPIR PSF is $p \times q$, then the extended FOV image has a length of $(m+p-1) \times (n+q-1)$. From the implementation perspective, for kth iteration, a gradient descent update is applied to the data fidelity term to get an intermediate solution v^k:

$$v^k = x^{k-1} - t[\hat{A}^T \hat{S}^T (\hat{S}\hat{A}x - y)]_{k-1}. \tag{6}$$

Here, $(.)^T$ represents the transport operator. Step size t is calculated using the back-tracking line search method. Once the intermediate solution is available, the proximal operator of the total variation is evaluated [22] to get the next guess solution:

$$x^k = \mathbf{prox}_{\mathrm{TV}\lambda^k}(v^k). \tag{7}$$

Applying the proximal operator involves solving a convex optimization problem given by

$$\mathbf{prox}_{\mathrm{TV}\lambda^k}(v^k) = \min\ \lambda \|x\|_{\mathrm{TV}} + \frac{1}{2} \| x - v \|_2^2 . \tag{8}$$

The parameter λ is initially selected (for the first outer iteration) to be 0.1 and is then adjusted as follows. After every outer iteration, the change in the solution due to the gradient descent step is first calculated as

$$d_1 = \| v^k - x^{k-1} \|_2^2, \tag{9}$$

and the change in solution due to the application of the proximal operator is evaluated as

$$d_2 = \| x^k - v^k \|_2^2 . \tag{10}$$

If the change d_2 is close to d_1, ($d_2 > 0.95 d_1$ in our case), parameter λ reduces by a factor 0.99, else the same λ is used in the next outer iteration. This choice of λ parameter adjusts the change in the intermediate solution v^k due to the proximal operation from iteration to iteration. To further accelerate the convergence speed of the algorithm, we employ the well-known Nesterov [25] update. In particular, the gradient descent update [in Eq. (6)] is applied to the solution with an additional momentum term:

$$u^k = x^k + \gamma_k (x^k - x^{k-1}), \tag{11}$$

with

$$\gamma_k = \frac{k}{k+3}, \tag{12}$$

and $u(0) = x(0)$ as suggested by Nesterov. In the following sections, the same algorithm described here is applied to various simulations and experiment.

4. SIMULATION RESULTS ON PSF DESIGN

To better comprehend how the extended FOV system functions, we take into account the image reconstruction performance for a number of factors, including the number of impulses in the MPIR, the relative spatial extent of MPIR, and the detector size. The simulations give clear instructions for practical system design as well as a solid grasp of the extended FOV concept. In the following, we present experimental findings based on these factors. For the simulation study, we used the typical Siemens star object represented over in a 256×256 pixel matrix.

A. Necessary Condition

While MPIR-like impulse response enables extended FOV image recovery, the extent and number of impulses in the MPIR need to follow certain conditions for an artifact-free reconstruction. The recorded data in our system are available over the limited detector area. As per Eq. (6), these limited detector data are extended to a region decided by convolution of the detector area with the transposed PSF $p(-\mathbf{r})$. This overlap area represents the union of detector space corresponding to various impulse positions [26]. We observe that the restored information depends on the degree of overlap within the detector area that is achieved in the transpose operation. A similar consideration also usually arises in SIM systems, where the reconstruction quality depends on the overlap between various Fourier bands [17]. For a given impulse distribution and sensor area, overlapping can be increased by increasing the number of impulses or reducing the extent of PSF. Increasing the number of impulses within a given extent brings object information from various regions into the detection domain, therefore increasing the data energy and hence the reconstruction quality. We term this extreme as the *information* regime. However, the overlapping of various regions of the object reduces the contrast in the data and therefore degrades the reconstructed image quality. Therefore, sufficient contrast in the data is required for a good quality image recovery. We name this extreme as the *contrast* regime. The PSF design requires a trade-off between these two regimes. To explain this concept better, we introduce a relative energy measure R to assess the object information in the detection domain:

$$R = \frac{||\hat{S}\hat{A}x||_2^2}{||\hat{A}x||_2^2}. \tag{13}$$

The quantity R is the ratio of energy in the scrambled data over the limited detector area and the total energy of scrambled data. Since $\hat{A}$ contains the optical system information, the loss due to the optical system such as lens imperfection and others cancels out in this parameter. Clearly, R can take values in the interval (0, 1). In traditional imaging systems with single-point impulse response and full detector area, the measure $R \to 1$.

In the present problem, this measure can also serve the equivalent role of restricted isometry property (RIP) commonly used in compressive sensing literature [27], which is not straightforward to evaluate for a given measurement configuration. In general, the number R above increases with the overlap area.

The second important consideration when designing an extended FOV imaging system is the contrast in the recorded data. As a given object gets scrambled by MPIR, the relative contrast C of the detector pixel values decreases. Since realistic detector readouts have a noise floor and bit quantization effects, reduction in C leads to undesirable artifacts in the reconstructed extended FOV image. We define the image contrast C as

$$C = \frac{\sigma}{\langle I_{\text{out}} \rangle}. \tag{14}$$

Here, σ is the standard deviation, and $\langle I_{\text{out}} \rangle$ is the mean of pixel values over the detector. An increase in the number of impulses in the MPIR essentially increases the correlation in the measurements, which manifests itself in the form of a reduced value of C. We remark that the design of an extended FOV system with MPIR therefore involves a trade-off between increased energy ratio R and reduction in contrast C. In what follows, we consider this trade-off regarding the number of impulses in MPIR and the spatial extent of impulses.

1. *Reconstruction Performance as a Function of Number of Impulses with Fixed Spatial Extent*

We first explore the performance of an extended FOV system with the number of impulses. For a given sensor size, the total extent of the MPIR is decided based on the desired FOV. In our simulation, for a given spatial extent of MPIR, we have added more impulses uniformly in the internal region as shown by dotted squares in Fig. 3(a). With the number of impulses, the object information from various regions starts overlapping in the detection domain, leading to an increase in the parameter R as shown in Fig. 3(b). The right hand side of Fig. 3(b) represents what we refer to as the *information regime* where a higher degree of information is available for reconstruction. However, the contrast in the data reduces with the number of impulses as shown in Fig. 3(c). The left side of Fig. 3(c) represents what we refer to as the *contrast regime* where high contrast in detector data leads to better image reconstruction. We illustrate these points with simulations.

We used the Siemens star of size (256×256) with 25 spokes as a test object. The detector size is half the object (128×128) and was kept constant throughout the simulations. Additionally, we made the PSF extent to be larger compared to the detector size, i.e., (191×191) pixels. Therefore, the reconstructed FOV is of size (318×318) pixels. In each simulated case, the limited detector data have Poisson noise corresponding to a light level of 10^5 photons/pixel. Figures 3(a1)–3(a3) show the three MPIRs used with increasing numbers of impulses. We want to emphasize that the number of impulses has been increased inward for a given extent of impulses. It will helps in comparing various cases since the effective FOV is constant in all cases. Figures 3(b1)–3(b3) show the corresponding detector overlap patterns depicting the union

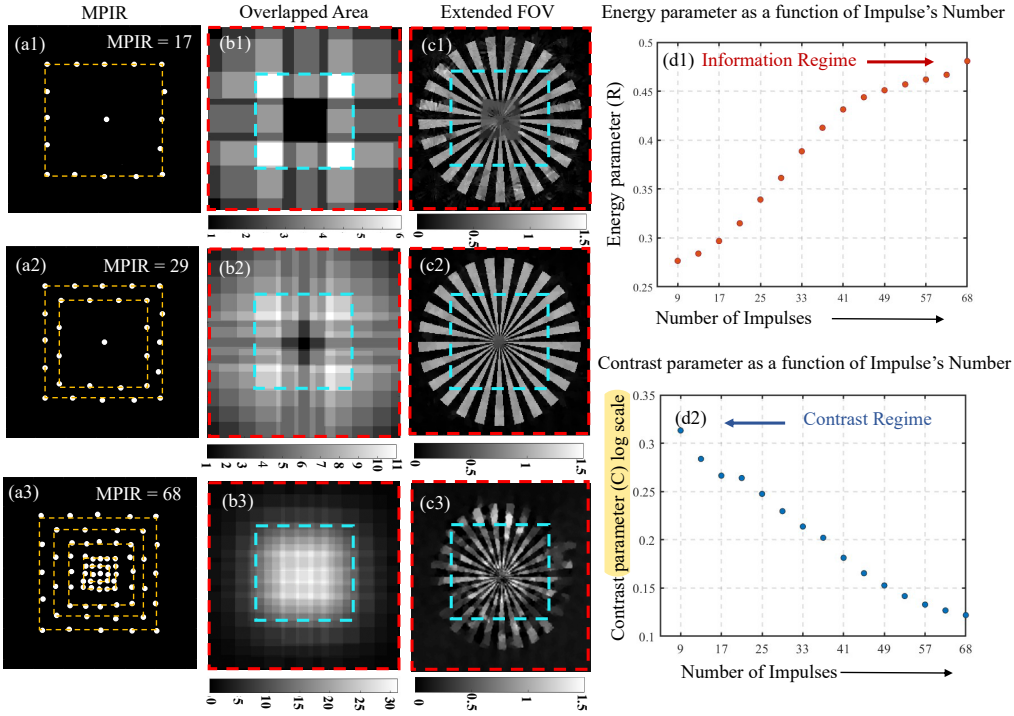

Fig. 3. Simulation of image reconstruction with varying numbers of impulses in a PSF. (a1)–(a3) MPIR with different impulses increased along the dotted yellow squares. Spatial variation in recovered information depends on the overlapped area in (b1)–(b3) with an effective FOV represented by the dotted red square. With the number of impulses, the information content of the reconstructed image increased (c1)–(c3) and therefore the energy parameter (d1) increases. The contrast parameter (d2) decreases and therefore leads to poor reconstruction quality (c3).

of detector space corresponding to various impulse positions. Finally, Figs. 3(c1) and 3(c2) show the corresponding image reconstructions obtained by using the reconstruction algorithm described in Section 2. When the number of impulses is low (= 17), we note that R is low, but the data have good contrast measured by the parameter C. Lower R is seen here to produce a reconstruction with artifacts, particularly in the region where the overlap is low. At the other extreme is the case where we use an MPIR with 68 impulses to increase R. However, the increase in R in this case is accompanied by a reduction in C. Practically recorded data will always have noise as well as bit quantization effects as simulated here. When the contrast C is low, the native fluctuations in the recorded intensity pattern can become comparable to noise and bit quantization effects at the detector. The reconstruction algorithm finds it difficult to handle these low contrast data, and the image quality is again seen to degrade the image quality. Therefore, it is reasonable to anticipate that an extended FOV computational imaging system will perform at its peak somewhere in the middle, as demonstrated for reconstruction using MPIR composed of 29 impulses. In fact, our simulations show that there is a range of number of impulse values for which the reconstructed image quality is seen to be comparable and quite good. For reference, the plots of the R and C parameters for various MPIRs used are shown in Figs. 3(d1) and 3(d2).

2. Reconstruction Performance as a Function of Extent of Impulses

In the next simulation study, we vary the extent of impulses relative to the detector size and investigate the reconstructed image quality for a fixed number of impulses in the MPIR design. We have fixed the number of 29 impulses in the MPIR for illustration. Figures 4(a1)–4(a3) show three cases of MPIR with extent smaller (64 × 64), comparable (128 × 128), and larger (256 × 256) compared to the detector area of (128 × 128) pixels, respectively. The blue and red dotted squares show the relative detector size and extended FOV, respectively. Figures 4(b1)–4(b3) show the overlap pattern calculated using the convolution of the active sensor area with the transposed MPIR $p(-\mathbf{r})$. As observed in the restored images in Figs. 4(c1)–4(c3), when the MPIR extent is smaller compared to the detector size, the overlap energy R is high but the extension of FOV is limited. To increase the FOV, if we increase the extent of impulses too much, the reconstructed image quality degrades due to a decrease in energy parameter R. The reconstructed image quality is poor for regions with low values in the overlap pattern. A good quality image reconstruction is obtained here when the extent of impulses is the same as the truncated detector size. The slight decrease in the plot of R for a small extent of impulses [left side of the plot in Fig. 4(d1)] is due to the fact that the extended FOV is not covering the whole object. The contrast parameter C shown in Fig. 4(d2) has an increasing trend with increasing MPIR extent. The minor fluctuations in

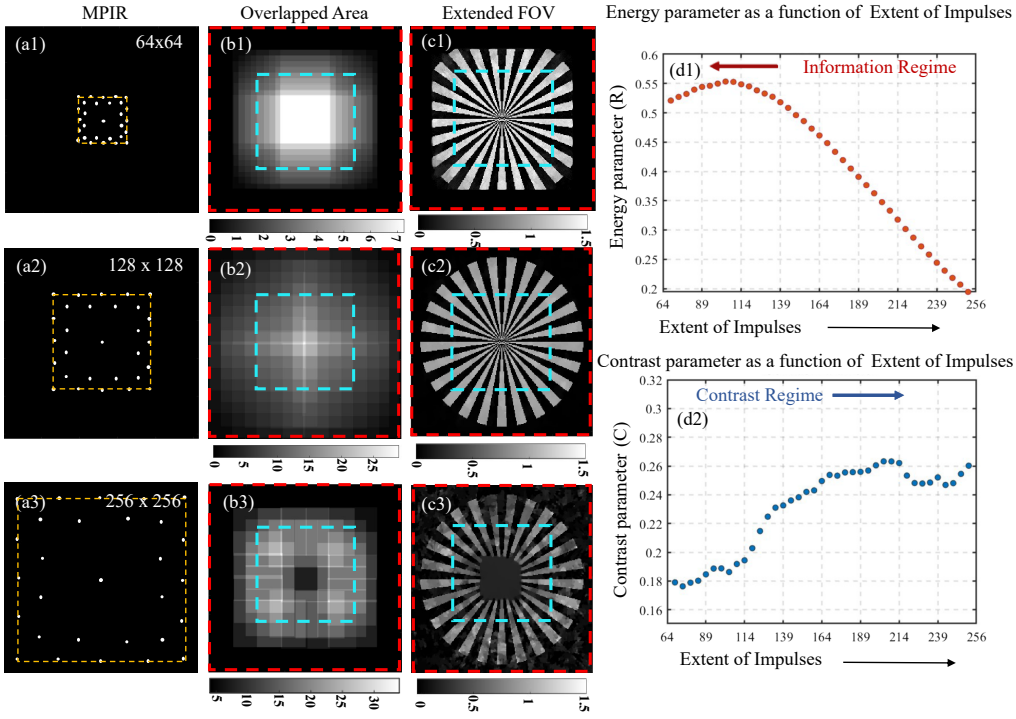

Fig. 4. Simulation of image reconstruction with the varying spatial extents of PSF. (a1)–(a3) MPIR with different PSF extents (shown by the dotted yellow squares): smaller (64 × 64), comparable (128 × 128), and larger (256 × 256) than the detector size of (128 × 128) pixels. Spatial variation in recovered information depends on the overlapped area in (b1)–(b3) with an effective FOV represented by the dotted red square. With the extent of PSF, the information content of the reconstructed image decreased (c1)–(c3) as seen in the plot of the energy parameter (d1). The slight decrease in the plot of R for small extent of impulses is due to the fact that the extended FOV is not covering the whole object. The contrast parameter (d2) has an increasing trend.

Table 1. Summary of Quantitative Performance of Simulated Reconstructions for the Illustrations Shown in Figs. 3 and 4

	Number of Impulses			Extent of Impulses		
	17	29	68	64 × 64	128 × 128	256 × 256
RMSE	0.27	0.09	0.53	0.67	0.06	0.45
PSNR	19	25	17	8.5	29	15
SSIM	0.86	0.96	0.61	0.68	0.99	0.71

the plot for C in Fig. 4(d2) are a function of the specific choice of object function and the arrangement of impulses in the MPIR.

We note an interesting feature of reconstructions in Figs. 3(c1) and 4(c3). In both cases, the reconstructed image near the center of the image is smoothed out in the central region where the corresponding overlap pattern has low weight. This is an artifact of the TV based reconstruction. We note that during the iteration, as per Eq. (6), when the error is backprojected from data space to object space, the region with low weight in the overlap pattern receives correspondingly low contribution. The TV penalty then causes blurring in this region as the relative signal and gradient magnitudes in this region are low. In Table 1, we summarize the results in Figs. 3 and 4 by providing the numerical values of quantitative image quality measures RMSE, PSNR, and SSIM for reconstructed images relative to the ground truth object used for simulations.

B. Sufficient Condition

If the detector spans the full FOV, i.e., whole scrambled data are utilized for the object reconstruction, then $R = 1$, and we may get high-quality object reconstruction [12] by direct Wiener filter based de-blurring. If the detector is truncated, then the reconstruction problem involves reconstructing an extended FOV from "incomplete" measurements. Such a reconstruction process needs to be performed via a sparse optimization procedure similar to what is explained in Section 3 or its variant. The sufficient condition is now therefore related to the compressive sensing theory. Nominally the number of measurements must be at least of the order of $3K \log(N/K)$ for a K-sparse object [28], for enabling an extended FOV system. Based on prior literature on compressive imaging, a typical pixel number gain in the range of three to five is reasonable to expect for the extended FOV imaging system. The simulations in Sections 4.A.1 and 4.A.2 suggest a practical trade-off between the energy parameter R and contrast parameter C that allows one to design the multiple point PSF. In the context of compressive sensing theory, a similar trade-off between the number of measurements and bit quantization of data has been studied in [29]. In general, it may be difficult to provide an ideal range of numerical values of these parameters, as the answer may depend on specifics of the system hardware, the applications at hand, and the class of objects under consideration. However, these parameters provide a methodology or a thought process that is useful for designing an extended FOV system. We have followed these guidelines in the experimental work discussed in the next section.

5. EXPERIMENTAL DEMONSTRATION

A. System Schematic

To validate the proposed extended FOV method, we considered a standard $4F$ system as shown in Fig. 5. A nearly spatially incoherent illumination is maintained using a 650 nm LED (Holmarc) along with a Köhler illumination technique for even illumination throughout the FOV. The illumination consists of a pair of 10× objectives (model: CFI E Plan Achromat 10×) that acts as a field lens and a collector lens to form an image of an LED filament at the front focal plane of the condenser lens. A 4× objective (model: CFI E Plan Achromat 4×) is used as a condenser lens that projects uniform illumination onto the object. Two convex lenses with focal length $f = 200$ mm make a $4F$ system with a reflective SLM device (Holoeye; model: Leto) in the Fourier plane. We have used phase modulation for Fourier plane aperture engineering since phase based design can allow asymmetric distribution of impulses. Practically, most SLM devices are therefore designed to operate in phase-only mode. Amplitude modulation can also be carried out along with phase modulation; however, amplitude modulation will lead to a decrease in the efficiency of diffraction order, which is an important factor in the experiment. A polarizer is placed in front of the SLM with the orientation along the preferred axis of the SLM device. A phase mask corresponding to the MPIR is generated using an inbuilt software of the SLM. A blazed grating [30] is added on the top of the phase mask to improve the diffraction efficiency of modulated light and with a period that can separate zeroth order from the modulated first order. The scrambled data are captured by a CMOS sensor (Lumnera; model: Lt945R, pixel size 3.45 μ). Other essential factors that must be considered in the experimental situation, such as the source's illumination intensity and the camera's exposure time. They are adjusted to ensure that the CMOS sensor does not show saturation.

The following illustrations use two regions (group 0 elements 4–6 and group 1 elements 1–4) of the standard USAF chart (Thorlabs; model:) as test objects. In our experiments, we used the MPIR with nine and 41 impulses, to ensure high-contrast data. The image of the test object at the first diffraction order is also captured without employing MPIR to ensure the baseline/or native resolution of the imaging system. We recorded the PSF in Figs. 6(a2) and 7(a2) using a pinhole object such as the PSF image observed in the first-order diffraction. A visual inspection of the PSF showed that the relative intensity of the impulses gradually decreased away from the zeroth order (not shown but located adjacent to the PSF region). We have accounted for this gradual decrease in impulse intensity in the PSF used for reconstruction. For this purpose, the PSF image was first thresholded, and the centroid of each of the regions was computed using the standard binary image processing tools available in the MATLAB image processing toolbox. To determine each impulse's strength, we computed the mean pixel value in a small circle centered at the centroid location of each of the impulses. The various impulses had relative strengths varying 1.0−0.7. Apart from the relative strength, each impulse is also not an ideal delta function but has a spread due to the diffraction limit of the finite system aperture, which we can account for in the reconstruction algorithm. Therefore, the

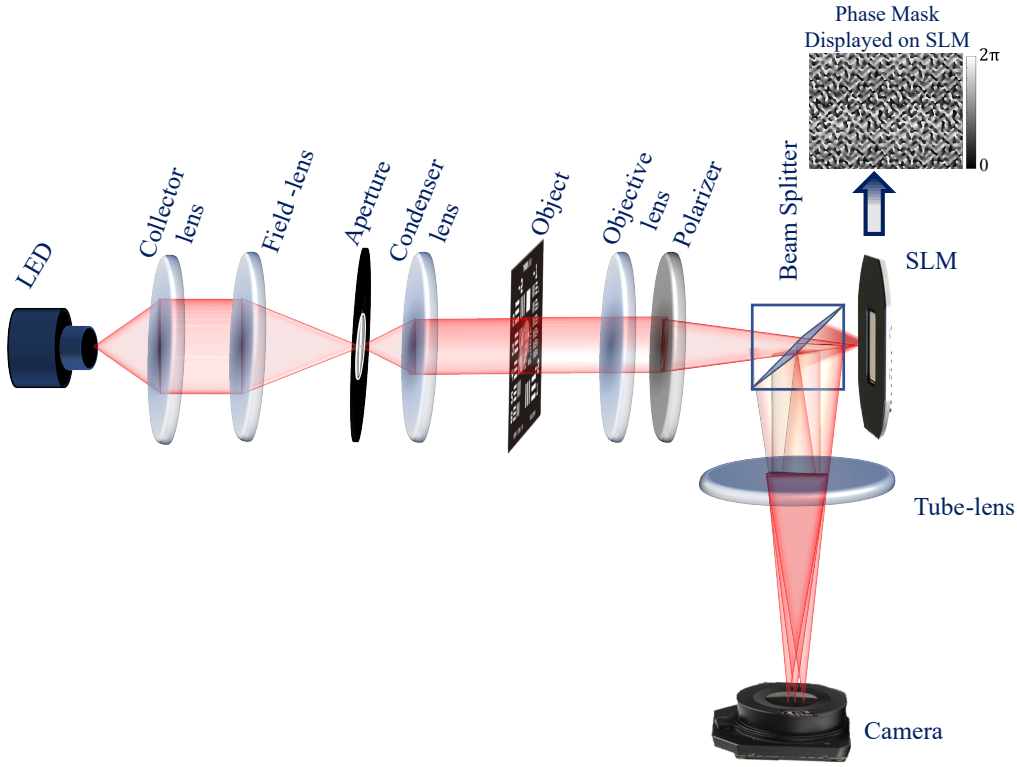

Fig. 5. Experimental setup for extended FOV system. A sample is illuminated uniformly using Köhler illumination with a spatially incoherent LED (650 nm) source. The part of the light modulated by the SLM is reflected by the beam splitter and forms a scrambled image onto the CMOS sensor.

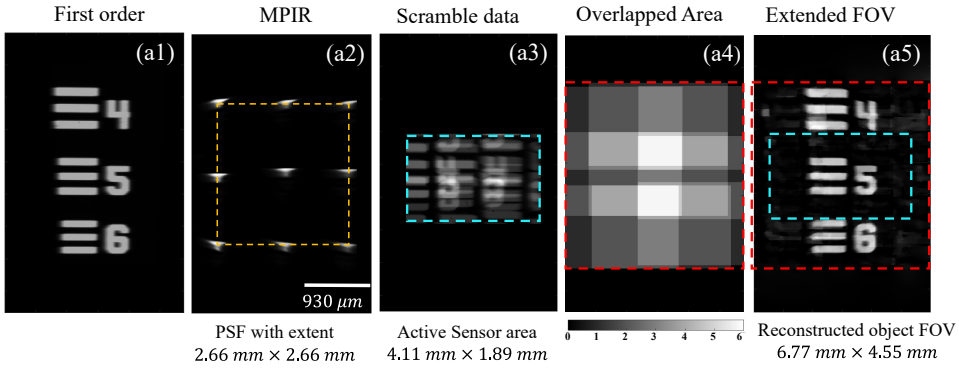

Fig. 6. Extended FOV results. (a1) Image recorded without MPIR coding in first order at native resolution of the system; (a2) MPIR captured using a pinhole object with nine impulses. The dotted yellow rectangle shows the PSF extent. (a3) Scrambled data captured by a small FOV sensor are shown in the blue rectangle. (a4) Overlapped area representing the spatial variation of recovered information with the dotted red square representing the effective FOV increment. (a5) Recovered extended FOV information beyond the blue square.

resolution of reconstructed images is essentially limited by the Fourier plane aperture.

We present two experimental validations of the extended FOV system concept in Figs. 6 and 7. Figures 6(a1) and 7(a1) show the native images on the camera that were recorded in the first order diffraction of the grating without the MPIR encoding. These images show the native imaging performance of the $4F$ system. The extended FOV illustrations use MPIRs of extent (614 × 597) pixels and (771 × 771) pixels, with physical extent of (2.12 mm × 2.06 mm) and (2.66 mm × 2.66 mm) as shown in Figs. 6(a2) and 7(a2), respectively. The number of impulses used in the two illustrations are nine and 41, respectively. Figures 6(a3) and 7(a3) show the limited detector record over a region of 4.11 mm × 1.89 mm and 3.11 mm × 1.89 mm within blue dotted rectangles, respectively, which was treated as spatially truncated raw data. The overlap patterns for the two cases are shown in Figs. 6(a4) and 7(a4), where the red dotted squares indicate the total extended FOV where we expect to obtain the reconstructed image. The corresponding reconstructions are shown in Figs. 6(a5) and 7(a5) and have physical extents of (6.77 mm × 4.55 mm) and (5.23 mm × 3.94 mm), respectively. We observe that the detector data have contrasts

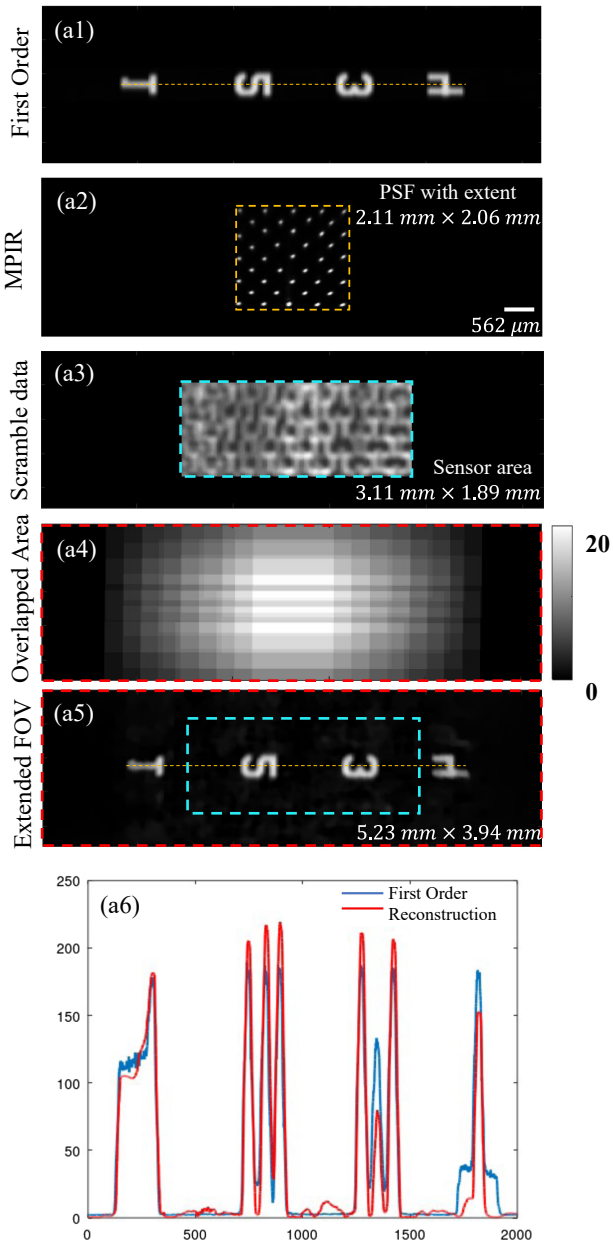

Fig. 7. Extended FOV results. (a1) Image recorded without MPIR coding in first order at native resolution of the system; (a2) MPIR captured using a pinhole object with 41 impulses. The dotted yellow rectangle shows the PSF extent. (a3) Scrambled data captured by a small FOV sensor are shown in the blue rectangle. (a4) Overlapped area representing the spatial variation of recovered information with the dotted red square representing the effective FOV increment. (a5) Recovered extended FOV information beyond the blue square. (a6) Profile plot through the dotted line in first-order image along with reconstruction for the resolution of the reconstructed image.

of 0.87 and 0.3, respectively, and nearly artifact-free extended FOV image reconstructions are possible. The resolution in the native image and the reconstructed extended FOV image are similar as well, as illustrated by the profile plot in Fig. 7(b). The illustrations in Figs. 6 and 7 suggest an extended FOV by a factor of approximately $2x$ in both directions without loss of resolution. Our simulations and experiments clearly bring out the requirements on balancing the various criteria associated with information gain via overlap and raw data contrast to enable an extended FOV computational imaging system.

6. CONCLUSION

In conclusion, we have reported an experimental demonstration of an extended FOV computational imaging system. The extended FOV imaging is achieved by a pupil phase mask corresponding to the MPIR system response. The system can be considered as a conjugate of a SIM concept where the roles of real and Fourier spaces have been exchanged. Unlike SIM, the extended FOV system is, however, capable of a single-shot imaging performance. The raw data recorded with such an imaging system consist of native images as well as information from an extended FOV (beyond the sensor boundary) in a scrambled form. The extended FOV image is reconstructed from these scrambled and incomplete data by a sparsity assisted optimization algorithm. In design of a practical extended FOV system, we find that two system design aspects play an important role. For a given physical extent of the MPIR PSF, increasing the number of impulses leads to information gain within the limited detector area, which improves the image reconstruction. An increase in the number of impulses, however, simultaneously reduces the contrast in the recorded raw data. It may become difficult to differentiate small variations in the raw data in the presence of detector noise and quantization effects. A balance between information gain and contrast reduction is therefore required for optimal image reconstruction performance. Additionally the local image quality over an extended FOV is dependent on the uniformity in the overlap pattern, which is a union of shifted truncated detector areas as per the transposed MPIR. We illustrate these points with simulations as well as experimental demonstrations that allow a nominal extension of the system FOV by a factor of 2× in both directions beyond the physical sensor boundary. The overall results illustrate an interesting extended FOV computational imaging system that highlights the role of information gain as well as detector precision. Our discussion of the system concept is quite general in nature and may apply to a number of incoherent optical imaging systems used in day-to-day consumer applications as well as scientific research.

Acknowledgment. RM acknowledges fellowship support from the Prime Minister Research Fellowship (PMRF), India. KK acknowledges partial support from Abdul Kalam National Innovation Fellowship of Indian National Academy of Engineering. Discussions with Prof. R. Elangovan on extended FOV imaging are acknowledged.

Disclosures. The authors declare no conflicts of interest.

Data availability. No data were generated or analyzed in the presented research.

REFERENCES

1. J. N. Mait, G. W. Euliss, and R. A. Athale, "Computational imaging," Adv. Opt. Photon. **10**, 409–483 (2018).
2. A. W. Lohmann, R. G. Dorsch, D. Mendlovic, Z. Zalevsky, and C. Ferreira, "Space–bandwidth product of optical signals and systems," J. Opt. Soc. Am. A **13**, 470–473 (1996).
3. S. Al-Janabi, A. Huisman, and P. J. Van Diest, "Digital pathology: current status and future perspectives," Histopathology **61**, 1–9 (2012).

4. C. V. Hutchinson, M. L. Brereton, and J. Burthem, "Digital imaging of haematological morphology," Clin. Lab. Haematol. **27**, 357–362 (2005).
5. D. J. Brady, M. E. Gehm, R. A. Stack, D. L. Marks, D. S. Kittle, D. R. Golish, E. M. Vera, and S. D. Feller, "Multiscale gigapixel photography," Nature **486**, 386–389 (2012).
6. G. Zheng, R. Horstmeyer, and C. Yang, "Wide-field, high-resolution Fourier ptychographic microscopy," Nat. Photonics **7**, 739–745 (2013).
7. G. McConnell, J. Trägårdh, R. Amor, J. Dempster, E. Reid, and W. B. Amos, "A novel optical microscope for imaging large embryos and tissue volumes with sub-cellular resolution throughout," eLife **5**, e18659 (2016).
8. T. Nakamura, R. Horisaki, and J. Tanida, "Computational superposition compound eye imaging for extended depth-of-field and field-of-view," Opt. Express **20**, 27482–27495 (2012).
9. Y. Peng, Q. Sun, X. Dun, G. Wetzstein, W. Heidrich, and F. Heide, "Learned large field-of-view imaging with thin-plate optics," ACM Trans. Graph. **38**, 219 (2019).
10. J. Park, D. J. Brady, G. Zheng, L. Tian, and L. Gao, "Review of bio-optical imaging systems with a high space-bandwidth product," Adv. Photon. **3**, 044001 (2021).
11. R. Malik, R. Elangovan, and K. Khare, "Computational imaging with an extended field of view," J. Opt. **23**, 085703 (2021).
12. B. J. Stossel and N. George, "Multiple-point impulse responses controlled blurring and recovery," Opt. Commun. **121**, 156–165 (1995).
13. E. R. Dowski and W. T. Cathey, "Extended depth of field through wave-front coding," Appl. Opt. **34**, 1859–1866 (1995).
14. W. Chi and N. George, "Optical imaging with phase-coded aperture," Opt. Express **19**, 4294–4300 (2011).
15. G. R. Arce, D. J. Brady, L. Carin, H. Arguello, and D. S. Kittle, "Compressive coded aperture spectral imaging: an introduction," IEEE Signal Process. Mag. **31**(1), 105–115 (2014).
16. A. Greengard, Y. Y. Schechner, and R. Piestun, "Depth from diffracted rotation," Opt. Lett. **31**, 181–183 (2006).
17. M. G. L. Gustafsson, "Surpassing the lateral resolution limit by a factor of two using structured illumination microscopy," J. Microsc. **198**, 82–87 (2000).
18. R. Horisaki and J. Tanida, "Multi-channel data acquisition using multiplexed imaging with spatial encoding," Opt. Express **18**, 23041–23053 (2010).
19. D. Marcos, T. Lasser, A. López, and A. Bourquard, "Compressed imaging by sparse random convolution," Opt. Express **24**, 1269–1290 (2016).
20. X. Yao, V. Pathak, H. Xi, A. Chaware, C. Cooke, K. Kim, S. Xu, Y. Li, T. Dunn, P. C. Konda, K. C. Zhou, and R. Horstmeyer, "Increasing a microscope's effective field of view via overlapped imaging and machine learning," Opt. Express **30**, 1745–1761 (2022).
21. A. Beck and M. Teboulle, "Fast gradient-based algorithms for constrained total variation image denoising and deblurring problems," IEEE Trans. Image Process. **18**, 2419–2434 (2009).
22. N. Parikh and S. Boyd, "Proximal algorithms," Found. Trends Optim. **1**, 123–231 (2013).
23. E. Y. Sidky and X. Pan, "Image reconstruction in circular cone-beam computed tomography by constrained, total-variation minimization," Phys. Med. Biol. **53**, 4777–4807 (2008).
24. M. Singh and K. Khare, "Single-shot interferogram analysis for accurate reconstruction of step phase objects," J. Opt. Soc. Am. A **34**, 349–355 (2017).
25. Y. Nesterov, "A method for solving the convex programming problem with convergence rate $o(1/k^2)$," Proc. USSR Acad. Sci. **269**, 543–547 (1983).
26. Y. C. Eldar, *Sampling Theory Beyond Bandlimited Systems* (Cambridge University, 2015).
27. E. J. Candes and M. B. Wakin, "An introduction to compressive sampling," IEEE Signal Process. Mag. **25**(2), 21–30 (2008).
28. R. G. Baraniuk, "Compressive sensing lecture notes," IEEE Signal Process. Mag. **24**(4), 118–121 (2007).
29. J. N. Laska and R. G. Baraniuk, "Regime change: bit-depth versus measurement-rate in compressive sensing," IEEE Trans. Signal Process. **60**, 3496–3505 (2012).
30. C. Rosales-Guzmán and A. Forbes, *How to Shape Light with Spatial Light Modulators* (SPIE, 2017).